The Astrophysical Journal, 871:45 (8pp), 2019 January 20 https://doi.org/10.3847/1538-4357/aaf4f2

Solar Polar Brightening and Radius at 100 and 230 GHz Observed by ALMA

Caius L. Selhorst[1], Paulo J. A. Simões[2,3], Roman Brajša[4], Adriana Valio[3], C. G. Giménez de Castro[3,5], Joaquim E. R. Costa[6], Fabian Menezes[3], Jean Pierre Rozelot[7], Antonio S. Hales[8,9], Kazumasa Iwai[10], and Stephen White[11]

[1] NAT—Núcleo de Astrofísica Teórica, Universidade Cruzeiro do Sul, São Paulo, SP, Brazil; caiuslucius@gmail.com
[2] SUPA School of Physics and Astronomy, University of Glasgow, G12 8QQ, UK
[3] CRAAM, Universidade Presbiteriana Mackenzie, São Paulo, SP 01302-907, Brazil
[4] Hvar Observatory, Faculty of Geodesy, University of Zagreb, Zagreb, Croatia
[5] IAFE, Universidad de Buenos Aires/CONICET, Buenos Aires, Argentina
[6] CEA, Instituto Nacional de Pesquisas Espaciais, São José dos Campos, SP, Brazil
[7] Université Côte d'Azur, 77 chemin des Basses Moulières, F-06130 Grasse, France
[8] Joint ALMA Observatory, Avenida Alonso de Córdova 3107, Vitacura 7630355, Santiago, Chile
[9] National Radio Astronomy Observatory, 520 Edgemont Road, Charlottesville, VA 22903-2475, USA
[10] Institute for Space-Earth Environmental Research, Nagoya University, Furo-cho, Chikusa-ku, Nagoya, 464-8601, Japan
[11] Space Vehicles Division, Air Force Research Laboratory, Albuquerque, NM, USA

Received 2018 July 15; revised 2018 November 28; accepted 2018 November 28; published 2019 January 21

Abstract

Polar brightening of the Sun at radio frequencies has been studied for almost 50 years and yet a disagreement persists between solar atmospheric models and observations. Some observations reported brightening values much smaller than the expected values obtained from the models, with discrepancies being particularly large at millimeter wavelengths. New clues to calibrate the atmospheric models can be obtained with the advent of the Atacama Large Millimeter/submillimeter Array (ALMA) radio interferometer. In this work, we analyzed the lower limit of the polar brightening observed at 100 and 230 GHz by ALMA, during its Science Verification period, 2015 December 16–20. We find that the average polar intensity is higher than the disk intensity at 100 and 230 GHz, with larger brightness intensities at the south pole in eight of the nine maps analyzed. The observational results were compared with calculations of the millimetric limb brightening emission for two semi-empirical atmospheric models, FAL-C and SSC. Both models presented larger limb intensities than the average observed values. The intensities obtained with the SSC model were closer to the observations, with polar brightenings of 10.5% and 17.8% at 100 and 230 GHz, respectively. This discrepancy may be due to the presence of chromospheric features (like spicules) at regions close to the limb.

Key words: Sun: chromosphere – Sun: general – Sun: photosphere – Sun: radio radiation

1. Introduction

In the solar atmosphere, a positive temperature gradient above the photospheric minimum temperature is expected (e.g., Vernazza et al. 1981; Fontenla et al. 1993), predicting an increase in brightness temperature from millimetric to centimetric wavelengths. To verify this prediction, many successful observations have been reported at frequencies between 17 and 860 GHz (see Selhorst et al. 2003, and references therein), with generally consistent results. In addition to the limb brightening, the radio observations at polar regions showed an intrinsic behavior, that was designated as polar brightening.

The great part of our knowledge about the polar brightening comes from the interferometric maps taken since 1992 at 17 GHz by the Nobeyama Radioheliograph (Nakajima et al. 1994, NoRH). Based on these maps, Shibasaki (1998) reported that regions near the solar poles showed brightness temperature values up to 40% above the quiet-Sun values, in contrast with equatorial limb regions having only 10% increase. This suggested that the presence of the polar brightening is associated with bright patches near the solar poles.

The 17 GHz polar brightening follows the faculae cycle (Selhorst et al. 2003) and polar magnetic field strength (Selhorst et al. 2011; Shibasaki 2013), which is anticorrelated with the sunspot cycle as reported by Efanov et al. (1980) at 22 and 37 GHz. Although bright patches and faculae occur at the poles, there is no one-to-one correlation between them (Gelfreikh et al. 2002). Nevertheless, they are frequently associated with the location of increased unipolar magnetic regions underlying the coronal holes (Gopalswamy et al. 1999; Brajša et al. 2007; Selhorst et al. 2010). This association was reinforced by Oliveira e Silva et al. (2016), who analyzed the polar behavior between 2010 and 2015 and found a good correspondence between the presence of coronal holes and polar brightening at 17 GHz.

The radio polar brightening is presumed to result from the atmospheric structure in this region. Observations at additional wavelengths are valuable because they probe different layers of the atmosphere: in particular, millimeter wavelengths probe deeper into the chromosphere. However, only few observations at millimeter/submillimeter wavelengths were performed and presented inconclusive results, that can be partially caused by the different antenna resolutions and the observational techniques employed. In the millimetric range, Pohjolainen et al. (2000) analyzed the standard R.A. and decl. maps observed by the Metsähovi antenna at 87 GHz (half-power beamwidth, HPBW = 60″) and reported that polar regions presented brightening increase of 0.5%–2%. Kosugi et al. (1986) used radial scans obtained with the Nobeyama 45 m telescope, and reported no polar brightening at 98 GHz (HPBW = 17″), but detected a polar brightening of 3%–7% at 36 GHz (HPBW = 46″), suggesting that the polar brightenings should be an upper chromospheric feature.

Approaching the submillimeter range, Horne et al. (1981) performed radial scans of the Sun with a single antenna of OVRO at 230 GHz (HPBW = 28″) and reported polar brightenings of 10% ± 5%.

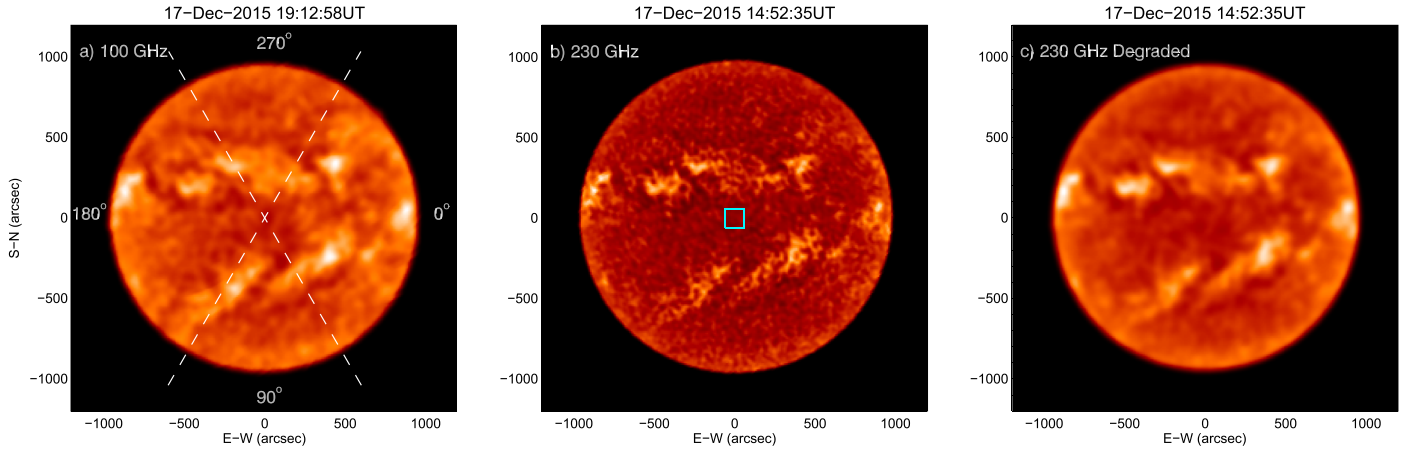

Figure 1. ALMA single-dish maps at 100 (a), 230 GHz (b), and the 230 GHz degraded to the 100 GHz resolution. The dashed lines in the panel (a) delimit the polar regions analyzed in this study, while the box in panel (b) sets the region used to calculate the quiet-Sun temperature.

Previous studies based on single-dish observations used radio telescopes with a large amount of broad sidelobes. Therefore, the limb study requires careful deconvolution of the sidelobe (e.g., Iwai & Shimojo 2015; Iwai et al. 2017).

Solar observations with the *Atacama Large Millimeter-submillimeter Array* (Wedemeyer et al. 2016) have started within its Cycle 4 of observations. The new observations at 100 and 230 GHz have already provided new insights about the solar atmosphere (White et al. 2017; Brajša et al. 2018), indicating a great potential for improvement in our understanding of the Sun.

Aiming to verify the presence of the polar brightening in the millimetric range, in this work we analyzed ALMA single-dish maps observed at 100 and 230 GHz during the Science Verification period in 2015 December. The same data set was used by Alissandrakis et al. (2017) to investigate the center-to-limb variation of the quiet Sun; however, the paper did not investigate the issue of the polar brightening, which is the specific focus of our paper.

As a secondary goal we also measured the solar radius using the ALMA solar maps. The photospheric radius has been measured for centuries while the measurements at radio wavelengths started only some decades ago. The solar radius is an important parameter for the calibration of solar atmospheric models and for a better understanding of the changes in the atmospheric structure. These measurements also show the altitude where most of the emission at the observed frequencies are generated.

We measured the polar brightening and estimated the solar radius. The results were compared with the solar atmospheric models proposed by Fontenla et al. (1993) and Selhorst et al. (2005a) and with previous observations at millimetric wavelengths.

2. ALMA Solar Maps

We analyzed ALMA fast-scan single-dish maps described by White et al. (2017). The data were observed during the Science Verification period, 2015 December 16–20, and released in the beginning of 2017.[12] The data comprise six maps obtained in Band 3 (84–116 GHz) and another three in Band 6 (211–275 GHz). In this work, we took 100 and 230 GHz as the reference frequencies for Bands 3 and 6, respectively. Since, these maps were obtained by a single-dish antenna of 12 m in diameter, they present nominal spatial resolutions of 58″ at 100 GHz and 25″ at 230 GHz (White et al. 2017). Figure 1 shows examples of the ALMA single-dish maps obtained at 100 GHz (a), 230 GHz (b), and the 230 GHz degraded to the same spatial resolution of the 100 GHz maps. The brightness temperature values, T_B, were scaled as T_B^4 to increase the contrast of features on the disk.

3. Data Analysis and Results

The polar brightening analysis was made in terms of the relative intensity above the quiet-Sun brightness temperature (T_{qS}). Following the method used by White et al. (2017), the T_{qS} of each map was assumed to be the mean brightness temperature of a small area at disk center (120″ × 120″, see Figure 1(b)), which is not affected by active regions. The obtained values and their respective errors are listed in Table 1. The T_{qS} at Band 3 maps presented a substantial variation between the observations made on the December 16 and 17, which may have affected the polar brightening results.

The maps obtained at 230 GHz were degraded in order to compare the observations with approximately the same resolution (Figure 1(c)). The degradation process was performed by the convolution of the Band 6 maps and a bidimensional Gaussian beam with 54″ (18 pixels), that was determined by the relation $\theta_{100}^2 = \theta_{230}^2 + \theta_x^2$, assuming that the ALMA observational beams are Gaussian.

Following Selhorst et al. (2003, 2011), the polar brightening was estimated from the average of 61 radial profiles through the disk center, that were taken every 1° between 60° and 120°, and between 240° and 300° position angles (corresponding to the south and north poles, respectively). The average profiles for the ALMA maps shown in Figure 1 are plotted in Figure 2(a), in which the dashed line represents the quiet-Sun intensity (T_{qS}).

Figure 2(b) shows in detail the average north pole profile (right side in Figure 2(a)) at Bands 3 and 6 (original and degraded). The dotted lines in Figure 2(b) present the measured polar brightening position. Due to the large differences in the spatial resolution, the radial position of the peak brightness at 100 GHz (896.″1) is ∼35″ closer to Sun center than at 230 GHz (931.″5); however, the brightness peak for the 230 GHz degraded profile is almost coincident with the 100 GHz profile.

[12] https://almascience.eso.org/alma-data/science-verification

Table 1
Average Polar Brightening and Measured Solar Radius

Map #	Day	Hr (UT)	Freq. (GHz)	T_{qS} (K)	Polar Brightening (lower limits)				Solar Radius (″)
					South		North		at $0.5T_{qS}$
					Intensity (%)	Position (″)	Intensity (%)	Position (″)	
1	2015 Dec 16	18:27:42	100	7560 ± 70	4.1 ± 2.1	890.2	3.0 ± 1.8	902.0	965.3 ± 3.2
2	2015 Dec 16	19:42:05	100	7370 ± 70	4.5 ± 2.1	884.3	2.9 ± 1.9	902.0	965.3 ± 3.1
3	2015 Dec 17	19:12:58	100	7100 ± 100	7.0 ± 2.8	854.8	6.3 ± 2.5	902.0	966.0 ± 3.3
4	2015 Dec 17	19:20:37	100	7080 ± 90	6.8 ± 2.6	854.8	6.2 ± 2.4	902.0	966.1 ± 3.1
5	2015 Dec 17	19:28:02	100	7070 ± 90	7.1 ± 2.7	854.8	6.2 ± 2.4	896.1	966.4 ± 3.0
6	2015 Dec 17	19:35:27	100	7110 ± 90	7.0 ± 2.5	860.7	6.2 ± 2.4	896.1	966.1 ± 3.2
7	2015 Dec 17	14:52:35	230	6210 ± 110	10.5 ± 3.4	931.5	9.1 ± 3.4	931.5	961.6 ± 2.6
8	2015 Dec 18	20:12:21	230	6350 ± 210	7.1 ± 4.7	931.5	7.9 ± 4.6	931.5	961.3 ± 1.7
9	2015 Dec 20	13:52:39	230	6270 ± 220	10.0 ± 5.2	931.5	9.2 ± 4.8	931.5	961.9 ± 2.0
10	2015 Dec 17	14:52:35	230*	6210 ± 50	8.3 ± 1.8	890.2	7.0 ± 1.4	896.1	964.1 ± 2.6
11	2015 Dec 18	20:12:21	230*	6310 ± 60	6.0 ± 1.9	890.2	6.6 ± 1.6	896.1	963.8 ± 1.4
12	2015 Dec 20	13:52:39	230*	6270 ± 80	7.3 ± 2.3	896.1	7.0 ± 1.8	896.1	964.4 ± 2.0

The difference in antenna beam spatial resolution is also responsible for the intensity reduction observed at lower resolutions (see Table 1).

A summary of the results can be seen in Table 1, in which the first three columns are the number reference, day, and hour of the observation, followed by observed frequency and brightness temperature of the quiet Sun T_{qS}. The maximum intensity and the position of the south and north average profiles are presented in the next columns, where the intensity uncertainty values are taken at maxima intensity positions. The last column shows the mean solar radius.

As can be verified in Table 1, the 100 GHz maps obtained on December 16th presented T_{qS} values larger than those observed on December 17th. Nevertheless, because our analysis was based on the relative intensities in each map, we decided to use all maps in the study. The average T_{qS} obtained for the six 100 GHz maps was 7220 ± 200 K, that is in agreement with the values suggested by White et al. (2017; 7280 ± 250 K) and Alissandrakis et al. (2017; 7250 K). At 230 GHz, the mean T_{qS} obtained for the three maps was 6280 ± 200 K, which is above the brightness temperature 5900 ± 190 K suggested by White et al. (2017); however, it is in agreement with the value obtained by Alissandrakis et al. (2017; 6180 K). The degradation of the 230 GHz has a small influence on the T_{qS} mean central temperature, but, as expected, it significantly reduces the standard deviation in which the averaged result was 6260 ± 80 K.

Except for the 230 GHz map obtained on December 18th, the south pole showed larger intensity values than the north pole; however, these differences are smaller than the standard deviation. The standard deviations of the polar brightening (Table 1) were calculated at the maximum of each average profile plus the T_{qS} uncertainty. For the six 100 GHz maps, the mean polar brightening values are $T_B/T_{qS} = 6.1\% \pm 2.8$ and $5.1\% \pm 2.7$, respectively, for the south and north poles. Moreover, both maps obtained on December 16th presented T_{qS} larger than those observed on December 17th, which could have underestimated polar brightening values. Nevertheless, as can be seen in Figure 5(a) the 100 GHz maps obtained on the same day presented a very similar mean profile.

The average of the three 230 GHz maps yield $T_B/T_{qS} = 9.2\% \pm 4.7$ for the south and $8.7\% \pm 4.4$ for the north pole intensities. Thus, the average polar brightening at 230 GHz is larger than the one at 100 GHz, probably due to the better spatial resolution. Furthermore, the 230 GHz maximum brightening occurred at the same position, i.e., the distance to the center of the solar disk, at both poles for all maps, which did not occur at 100 GHz. As can be seen in Figure 5(a), the south pole observed at 100 GHz on December 17 (maps #3–6) presented maxima far from the expected limb that is caused by the presence of bright features in the solar disk, which cannot be separated from the limb brightening due to the large beam (Selhorst et al. 2017).

For the degraded 230 GHz maps the results are compatible with those obtained at 100 GHz inside the standard deviations, in which the mean polar brightening values are $T_B/T_{qS} = 7.2\% \pm 2.2$ and $6.9\% \pm 1.6$, respectively for the south and north poles.

The solar radius of each map was also determined to verify the variation caused by the limb brightening and its convolution with the antenna beam size. Following Costa et al. (1999), the radius was determined at the point in which the brightness temperature drops to 50% of the T_{qS} value. The procedure to obtain the radius was similar to the one used in Selhorst et al. (2011), which can be summarized as follows: (a) determination of T_{qS}; (b) solar limb position determined by `contour` procedure of IDL at the level equal to half of T_{qS}; (c) 1440 points determined over the curve resulting from step b; (d) a circumference fit adjusted to the points. The obtained solar radius values presented mean values of 965.″9 ± 3.″2 at 100 GHz and 961.″6 ± 2.″1 at 230 GHz. These measurements are larger than the mean values obtained at the inflection point by Alissandrakis et al. (2017), but agree within the standard deviations. Moreover, the mean radius at 230 GHz also agrees with the averaged value obtained by Menezes & Valio (2017) at 212 GHz (966.″5 ± 2.″8). As expected, the degradation of the 230 GHz maps increases their radii to an averaged value of 964.″1 ± 2.″1.

4. Atmospheric Models

In a recent report, Alissandrakis et al. (2017) analyzed the center-to-limb variation of the same set of ALMA maps studied here and suggested that the observations were best fitted by the average quiet-Sun model C (FAL-C) proposed by Fontenla et al. (1993). Thus, we calculated the FAL-C brightness

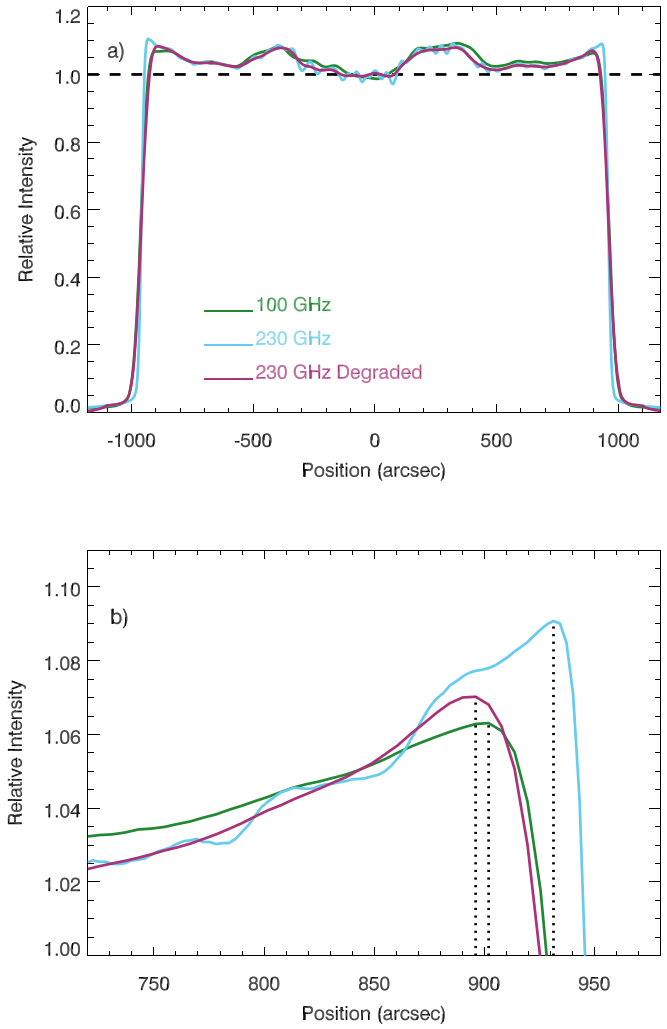

Figure 2. (a) Comparison between the averaged polar profiles obtained at 100 GHz (red) and 230 GHz (blue, and degraded in pink), in which the dashed line represents the quiet-Sun intensity. (b) Detail of the average north pole profile at both frequencies, as well as the degraded profile. The dotted lines indicate the measured polar brightening position.

temperature variation from the center-to-limb, where the H free–free opacity (κ_ν(H)) as well as the H^- free–free opacity ($\kappa_\nu(H^-)$) were considered, that can become significant at submillimetric wavelengths.

The observed polar brightenings were also compared with atmospheric model SSC proposed by Selhorst et al. (2005a), which follows the FAL-C temperature and density (H, electron, and ions) distributions up to 1000 km above the solar surface; however, for a good fit at radio wavelengths, the authors considered an extended chromosphere, in which the base of the transition region is kept at 3500 km, as in the Zirin et al. (1991) model. This extended chromosphere is proposed to address the mean contribution of the chromospheric features unresolved by radio observations, such as spicules. The SSC model also considers a coronal plasma up to 40,000 km above the solar surface. The same corona was included in the FAL-C model in order to estimate the coronal contribution to the limb brightening at ALMA Bands 3 and 6 (100 and 230 GHz respectively). Figure 3 shows the comparison between the temperature and density distributions proposed by the FAL-C and SSC atmospheric models. It is necessary to take into

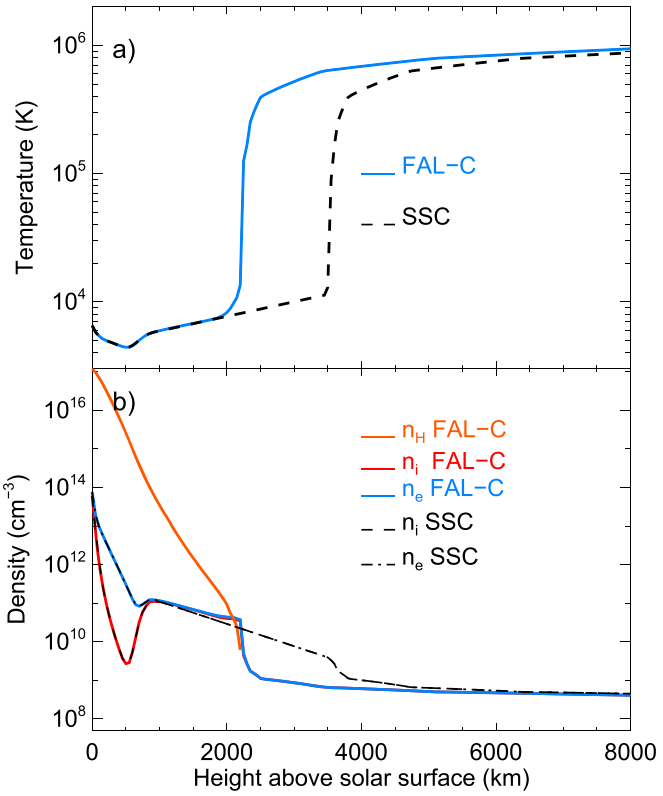

Figure 3. (a) Temperature and (b) densities (n_e, n_i, and n_H) distributions for the FAL-C and SSC atmospheric models.

account that the main purpose of these models is to reproduce the brightness temperature of solar disk center and they do not consider the special features observed at the polar regions.

The same equations used in Simões et al. (2017) to calculate κ_ν(H) and $\kappa_\nu(H^-)$ (in cm^{-1}) were adopted here, as follows:

$$\kappa_\nu(\mathrm{H}) = 3.7 \times 10^8 T^{-1/2} n_e n_i \nu^{-3} g_{ff}, \quad (1)$$

where the n_e and n_i are the electron and proton densities, respectively, T is the electron temperature and g_{ff} is the Gaunt factor, numerically obtained by van Hoof et al. (2014).

Following Kurucz (1970), the H^- free–free opacity is calculated by:

$$\kappa_\nu(H^-) = \frac{n_e n_\mathrm{H}}{\nu}(A_1 + (A_2 - A_3/T)/\nu), \quad (2)$$

where n_H is the neutral hydrogen density, and the numerical coefficients are $A_1 = 1.3727 \times 10^{-25}$, $A_2 = 4.3748 \times 10^{-10}$, and $A_3 = 2.5993 \times 10^{-7}$.

The total opacity is given by

$$\kappa_\nu = [\kappa_\nu(\mathrm{H}) + \kappa_\nu(H^-)](1 - e^{-h\nu/k_b T}), \quad (3)$$

with the term $(1 - e^{-h\nu/k_b T})$ being the correction for stimulated emission, where h and k_b are the Planck and Boltzmann constants, respectively.

Then, the optical depth is determined by $\tau_\nu = \int \kappa_\nu ds$. The formation height of emission is given by the contribution function (CF, given in erg s^{-1} cm^{-3} Hz^{-1} sr^{-1} throughout this paper), which is defined as

$$\mathrm{CF}(h) = j_\nu e^{-\tau_\nu}, \quad (4)$$

Table 2
Atmospheric Models Results

Model	Freq. (GHz)	T_{qS} (K)	Limb Brightening						Solar Radius (″)		
			Intensity (%)			Position (″)			at $0.5T_{qS}$		
	HPBW (″)		0.14	25	58	0.14	25	58	0.14	25	58
FAL-C [κ_ν(H)]	100	7670	79.6	23.1	15.8	962.7	939.9	909.3	962.8	966.6	970.2
FAL-C [κ_ν(H) + κ_ν(H$^-$)]	100	7670	79.6	23.1	15.8	962.7	939.9	909.3	962.8	966.6	970.2
SSC [κ_ν(H)]	100	7180	33.7	14.6	10.5	963.2	939.5	906.6	964.3	966.7	969.1
FAL-C [κ_ν(H)]	230	6220	73.5	20.2	14.7	962.5	938.5	905.7	962.8	966.0	969.1
FAL-C [κ_ν(H) + κ_ν(H$^-$)]	230	6190	74.3	20.7	15.2	962.5	938.5	905.9	962.8	966.1	969.2
SSC [κ_ν(H)]	230	5970	37.3	17.8	13.3	962.4	939.0	906.0	963.6	966.2	968.9

where $j_\nu = \kappa_\nu B_\nu(T)$ is the emission coefficient, and $B_\nu(T)$ is the Planck function.

The brightness temperature as a function of the wavelength is calculated as:

$$T_B(\nu) = \int T\kappa_\nu e^{-\tau_\nu} ds. \quad (5)$$

The brightness temperature calculated for the 1D model distributions, plotted in Figures 3(a) and (b), are assumed as the T_{qS}. If only the free–free opacity, κ_ν(H), is considered, the FAL-C model gives $T_{qS} = 7670$ K at 100 GHz and $T_{qS} = 6220$ K at 230 GHz. The inclusion of the H$^-$ free–free opacity did not change the 100 GHz value, and a small reduction in the value at 230 GHz, namely, 6190 K. For the SSC model (κ_ν(H) only), the results were $T_{qS} = 7180$ and 5970 K, at 100 and 230 GHz, respectively. These results are summarized on Table 2.

The optical depth at 100 GHz is showed in Figure 4(a) by the curves salmon, green, and dotted–dashed. The $\tau_\nu = 1$ layer occurs in the chromosphere around ∼1550 km and ∼1650 km above the solar surface, respectively, in the SSC and FAL-C models. At these heights the opacity is completely dominated by H free–free. The 100 GHz CF (Figure 4(b)) reaches a maximum around 1500 km in the SSC model, and presents relatively constant values between 1650 and 2100 km in the FAL-C model. Since the $\tau_\nu = 1$ layer for the FAL-C model is around 1650 km, it is clear that the emission formed above this height is optically thin.

At 230 GHz, inspecting the contribution function CF (Figure 4(b)), the emission is formed mainly at two different layers: near the temperature minimum region ($h < 400$ km) and in the chromosphere (roughly between $800 < h < 1500$ km). The optical depth τ_ν at 230 GHz (Figure 4(a), red, purple, and dashed curves) reaches $\tau_\nu \gg 1$ around photospheric temperature minimum ($h < 400$ km). From the contribution function CF, it is clear that the height of formation of the emission is slightly altered when the H$^-$ opacity is considered. The chromospheric peak of the 230 GHz CF is formed by H free–free radiation, and it is not completely optically thin ($\tau_\nu \sim 1$) or optically thick: the photospheric contribution is still visible through the chromosphere, if the observation is made at solar disk center.

Following Selhorst et al. (2005a), to calculate the limb brightening, the atmospheric models (Figures 3(a) and (b)) were expanded as 2D matrices, representing one quadrant of the Sun by taking into account the solar curvature ($R_\odot = 696$ Mm or 959.″64). Each matrix pixel represents an area of 50×50 km^2. To verify the sharpness of the limb brightening, the brightness temperature was computed every 100 km in the center-to-limb direction, and these results convolved with a Gaussian function with the same resolutions of the observed maps, i.e., 25″ and 58″.

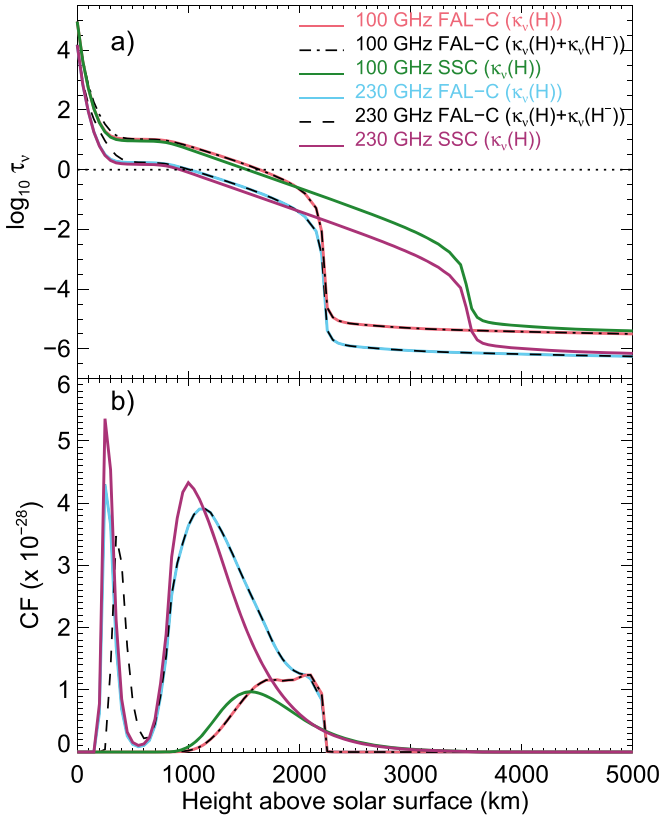

Figure 4. Panel (a) shows the variation of the optical depth (τ_ν) with the height above the solar surface, in which the horizontal dotted line represents $\tau = 1$. The variation of the contribution function (CF) with the height above the solar surface is plotted on (b).

The FAL-C high-resolution calculation yields very intense limb brightenings, with a peak of 79.6% at 100 GHz, for both scenarios, i.e., considering or not the H$^-$ absorption. Due to their sharp aspect, after the 25″ and 58″ Gaussian-beam convolution, these maximum limb brightening values were severely reduced to 23.1% and 15.8%, respectively. At 230 GHz, the inclusion of the H$^-$ absorption does not change the maximum brightness temperature value ($T_{B_{\max}}$), however, due to the small reduction in the T_{qS} caused by its inclusion, the maximum percentages do show a small difference, namely, 73.5% and 74.3%; however, after the beam convolution, the intensities were reduced to 20.2% and 20.7% for a 25″ beam and 14.7% and 15.2% for 58″ beam. In the raw profiles,

maximum $T_{B_{\max}}$ occurred at the transition region base for both frequencies, which caused an abrupt intensity decrease after the maxima, dropping from the maximum value to $0.5T_{qS}$ in less than 200 km.

On the other hand, the high-resolution SSC calculations presented smaller maximum temperature values than the FAL-C results. Moreover, the SSC calculations at 230 GHz show larger T_B/T_{qS} limb values (37.3%) than at 100 GHz (33.7%), which is the opposite of the high-resolution results for FAL-C. For both bands, the SSC limb maximum occurred in the middle of the prolonged chromosphere proposed in the model, which resulted in a gradual T_B decrease after the maximum at both Bands. The SSC brightness temperature values dropped from the $T_{B_{\max}}$ to $0.5T_{qS}$ in ~900 km.

Given the more gradual spatial decrease in brightness temperature in the SSC model, after the $T_{B_{\max}}$, the Gaussian-beam convolution resulted in smaller reduction of T_B in comparison with FAL-C simulations. After the convolution with a 25″ beam, the SSC limb brightening intensities were 14.6% and 17.8% above the T_{qS}, respectively, at 100 and 230 GHz. The convolution with a 58″ Gaussian-beam resulted in limb intensities of 10.5% at 100 GHz and 13.3% at 230 GHz.

In Figure 5, we compare the profiles obtained for the models SSC and FAL-C (only κ_ν(H)) and the observed T_B mean profiles obtained from the ALMA maps #3, #7, and the degraded #10 on Table 1. The light blue shadow around the observational mean profile represents the standard deviation of each point, which includes the T_{qS} uncertainty. Regarding the 100 GHz model, the SSC and the FAL-C profiles detached from one another toward the limb (Figure 5(a)), at 230 GHz, the SSC profile mimics the FAL-C with a smaller T_B (Figures 5(b) and (c)).

The more intense and larger limb brightening obtained in FAL-C also reflects on the position of the limb brightening maximum and the solar radius at $0.5T_{qS}$. As shown in Table 2, for the raw SSC simulations at 100 GHz the maximum T_b position occurred at 963.″2, whereas FAL-C presents the maximum 0.″5 smaller, 962.″7. Nevertheless, after the Gaussian-beam convolution the positions are reversed, for the 58″ beam the SSC maximum occurred on 906.″6, while for the FAL-C, the maximum was located on 909.″3. The 100 GHz SSC radius increased from 964.″3 on the raw simulation to 969.″1 after the convolution with the 58″ beam, while on the FAL-C, the radius increased from 962.″8 to 970.″1. The same behavior was detected on the 230 GHz radius.

In comparison with the observations (see Figure 5), both models presented larger $T_{B_{\max}}$ than the observed mean values at both frequencies. Still, the shape of the simulated center-to-limb profiles generally agrees with the observations when the uncertainties are considered.

5. Discussion and Conclusions

In this work, we report the analyses of the polar brightening observed in the ALMA single-dish maps at 100 and 230 GHz. Although the sidelobe level of the ALMA total power antenna should be lower than that of the previous antenna, there should be nonzero sidelobes in a radio telescope beam. Therefore, the derived polar brightening should be a lower limit. The polar brightenings at 100 GHz are $T_B/T_{qS} = 6.1\% \pm 2.8$ and $5.1\% \pm 2.7$, respectively, for the south and north poles. At 230 GHz, the mean values are $T_B/T_{qS} = 9.2\% \pm 4.7$ for the south and $8.7\% \pm 4.4$ for the north poles. For the 230 GHz maps degraded to the 100 GHz resolution, the polar brightenings reduced to $7.2\% \pm 2.2$ and $6.9\% \pm 1.6$, respectively for the south and north poles. The south pole showed larger brightening values, which may reflect the presence of a small coronal hole, which is known to have small bright structures (Gopalswamy et al. 1999; Brajša et al. 2007; Oliveira e Silva et al. 2016). Nevertheless, the difference between the poles is smaller than the standard deviation and will need more observations to verify the coronal hole influence on the polar brightening at these frequencies.

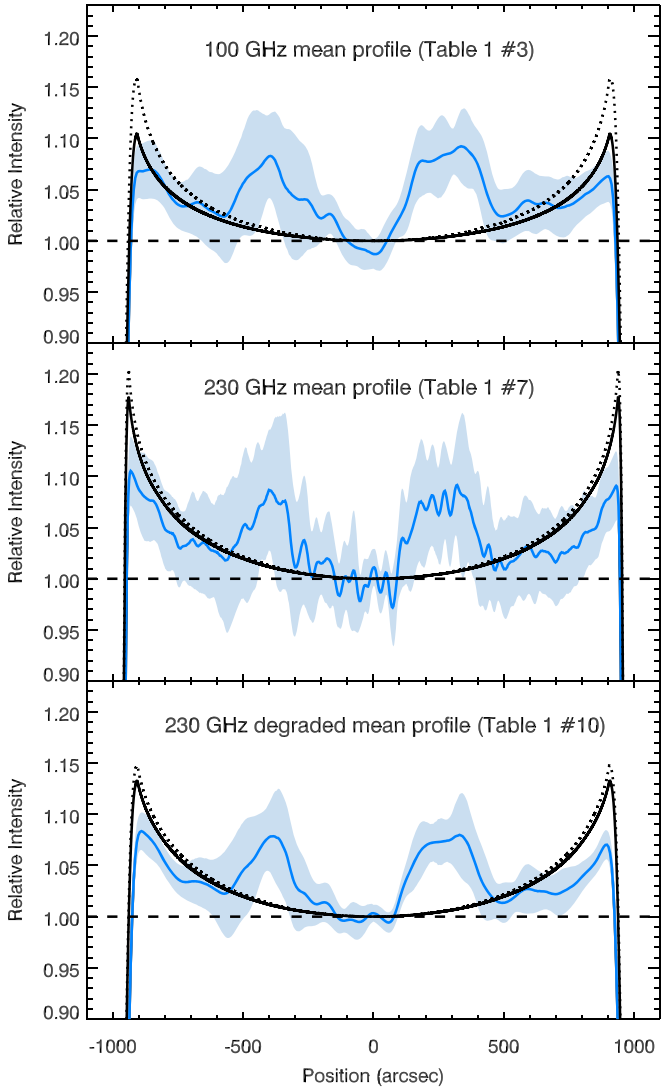

Figure 5. Comparison between observed brightness temperature mean profiles (blue curves) and the atmospheric models FAL-C (dotted lines) and SSC (continuous black lines). The dashed line represents the quiet Sun. The light blue shade around the observational mean profile represents the standard deviation of each point, which includes the T_{qS} uncertainty.

In comparison with the previous results at Band 3 (84–116 GHz), the results at 100 GHz are larger than the 0.5%–2% at 87 GHz reported by Pohjolainen et al. (2000). At Band 6 (211–275 GHz), our results are in agreement with those observed by Horne et al. (1981) ($10\% \pm 5\%$) at 230 GHz.

The averaged solar radii obtained were $965.''9 \pm 3.''2$ at 100 GHz, $961.''6 \pm 2.''1$ for the original 230 GHz maps, and $964.''1 \pm 2.''1$ after their degradation. These values agree with those deduced from the inflection point method used by Alissandrakis et al. (2017), and also agree with the average

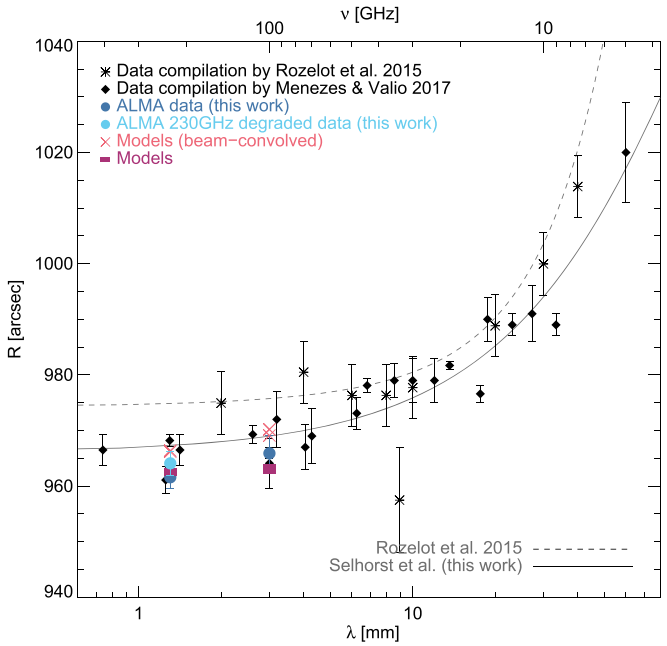

Figure 6. Mean solar radius from measurements at 100 and 230 GHz with other radio measurements collected by Rozelot et al. (2015) and Menezes & Valio (2017). These historical data were obtained with distinct spatial resolutions and methods. The radii obtained with the models are also shown.

value obtained by Menezes & Valio (2017) at 212 GHz, within standard deviations. The increase of 230 GHz in radius after the degradation reflects the great contribution of the intense limb brightening. If it was absent, the radius obtained at $0.5T_{qS}$ should not be dependent on the antenna beam resolution.

In Figure 6 we combine the historical data compiled by Rozelot et al. (2015) and Menezes & Valio (2017), also including our own results from ALMA observations. Above ≈50 GHz, our results, along with the recent results compiled by Menezes & Valio (2017), suggest smaller radii at these frequencies than previously suggested by Rozelot et al. (2015). The continuous curve in Figure 6 shows our simple polynomial fit (order 2) to all data shown, while the dashed curve represents a similar curve obtained by Rozelot et al. (2015). Although these curves may emphasize the height above the photosphere at which the solar radius is determined, due to the distinct spatial resolution that the radii were obtained, we do not claim that they represent any physical characteristics of the solar radius but are proposed as a simple visualization guide of the typical values of the radii measured at radio frequencies.

The observational results were contrasted with the atmospheric models FAL-C (Fontenla et al. 1993) and SSC (Selhorst et al. 2005a). For the FAL-C model, the H and H^- free–free opacities were considered. The results showed that the H^- absorption does not affect the quiet-Sun emission at 100 GHz but changes the emission at 230 GHz in only 30 K. The T_{qS} obtained by FAL-C, 7670 K at 100 GHz, is higher than the upper limit of the observed values obtained here (7220 ± 200 K). At 230 GHz the model resulted in 6220 K or 6190 K (with H^-), which are in agreement with the observational result 6280 ± 200 K, but higher than the upper limit of that suggested by White et al. (2017; 5900 ± 190 K). The T_{qS} overestimation by the FAL-C at radio frequencies has been previously reported in the centimeter range between 1 and 18 GHz (Bastian et al. 1996). On the other hand, the SSC presented $T_{qS} = 7180$ K at 100 GHz and $T_{qS} = 5970$ K at 230 GHz, in agreement with the values suggested by White et al. (2017) and the observed values at 100 GHz. However, the mean T_{qS} value observed at 230 GHz is larger than that obtained in the observations.

All atmospheric models predicted limb brightening intensities larger than the observed ones. However, when the beam sizes were considered, the SSC model yields values closer to the observations, 10.5% at 100 GHz and 17.8% and 13.3% at 230 GHz, respectively, for the original and degraded maps. When compared with observed mean brightness profiles, both models presented are in better agreement with the observations at 230 GHz (Figure 5(b)). At 100 GHz, however, the FAL-C limb brightening is much broader than the SSC model and the observed profiles. These discrepancies between the observational and model results can be caused by the different spatial resolutions and sidelobe levels of the telescopes. Since, we considered only the main beam of the telescope and that the observational result should contain the sidelobe effect, if the sidelobes could be convolved to the atmospheric models or even removed from the observations, the agreement between the model and the observational results, will probably be better.

The intense limb brightenings obtained by the models also enlarge the solar radius estimated at $0.5T_{qS}$, making them larger than the observed ones. Besides their larger values, the modeled radii are in agreement with the previous observations shown in Figure 6. The recent data included in Figure 6 resulted in a new adjusted curve with smaller values than that suggested by Rozelot et al. (2015). The historical results included in Figure 6 were measured at different phases of the solar cycle, which also may affect the radius at radio frequencies (Selhorst et al. 2011; Menezes & Valio 2017). In any case, facing the difficulty to obtain the radio observation data, together with their calibration, the results obtained so far show a rather good agreement with the model and deserve to be described.

Another difference between the observations and models is the position of the maximum limb brightening. At 230 GHz the maximum position is similar for all maps at both poles, located at 931.″5 from the disk center, which is ∼7.″5 smaller than the modeled position (∼939″). On the other hand, at 100 GHz, the modeled position varies from 906.″6 for the SSC and 909.″3 for FAL-C, while the observations at the north pole showed peak positions of 896″ or 902″ (the difference is only the pixel size), and ∼855″ at the south pole. Such smaller radius measurements are probably due to the presence of bright features close to the limb, that are merged with the usual limb brightening (Selhorst et al. 2017). Moreover, the limb location may also be affected by the difference of the sidelobes of the telescopes.

Despite the discrepancy with the models, our results are the best we can do with these data, but higher resolution data may produce refined results for the location and magnitude of any brightening.

Finally, the observational results listed above are in agreement with those reported by Alissandrakis et al. (2017). However, the SSC model presented limb brightening temperatures closer to the observations, than the values obtained with the FAL-C, which should have the best observational fit between the FAL models (Alissandrakis et al. 2017). The SSC limb brightening temperature reduction may be due to the prolonged chromosphere, which represents a mean contribution of the unresolved features, like spicules, that guide the chromospheric plasma to coronal heights. This more extended chromosphere contributes to absorption of the submillimeter

emission formed at the base of the chromosphere reducing the brightness temperature. Moreover, the presence of these chromospheric features at the regions close to the limb can hardly change the mean temperature profile presented here (Selhorst et al. 2005a, 2005b, 2017) and will be simulated in a future work. Further investigation can be possible through the modeling of the broad sidelobe (e.g., Iwai et al. 2017) and implementation of the sidelobe deconvolution.

C.L.S. acknowledges financial support from the São Paulo Research Foundation (FAPESP), grant number 2014/ 10489-0. P.J.A.S. acknowledges support from the University of Glasgow's Lord Kelvin Adam Smith Leadership Fellowship. A.V. and F.M. acknowledge partial funding from Fapesp. R.B. acknowledges partial support by Croatian Science Foundation under the project 6212 "Solar and Stellar Variability". This paper makes use of the following ALMA data: ADS/JAO. ALMA#2011.0.00020.SV. ALMA is a partnership of ESO (representing its member states), NSF (USA) and NINS (Japan), together with NRC (Canada) and NSC and ASIAA (Taiwan), and KASI (Republic of Korea), in co-operation with the Republic of Chile. The Joint ALMA Observatory is operated by ESO, AUI/NRAO, and NAOJ. The National Radio Astronomy Observatory is a facility of the National Science Foundation operated under cooperative agreement by Associated Universities, Inc.

ORCID iDs

Caius L. Selhorst https://orcid.org/0000-0002-5897-5236
Paulo J. A. Simões https://orcid.org/0000-0002-4819-1884
Adriana Valio https://orcid.org/0000-0002-1671-8370
C. G. Giménez de Castro https://orcid.org/0000-0002-8979-3582
Joaquim E. R. Costa https://orcid.org/0000-0002-0703-4735
Fabian Menezes https://orcid.org/0000-0002-4703-4027
Jean Pierre Rozelot https://orcid.org/0000-0002-5369-1381
Antonio S. Hales https://orcid.org/0000-0001-5073-2849
Kazumasa Iwai https://orcid.org/0000-0002-2464-5212
Stephen White https://orcid.org/0000-0002-8574-8629

References

Alissandrakis, C. E., Patsourakos, S., Nindos, A., & Bastian, T. S. 2017, A&A, 605, A78
Bastian, T. S., Dulk, G. A., & Leblanc, Y. 1996, ApJ, 473, 539
Brajša, R., Benz, A. O., Temmer, M., et al. 2007, SoPh, 245, 167
Brajša, R., Sudar, D., Benz, A. O., et al. 2018, A&A, 613, A17
Costa, J. E. R., Silva, A. V. R., Makhmutov, V. S., et al. 1999, ApJL, 520, L63
Efanov, V. A., Moissev, I. G., Nesterov, N. S., & Stewart, R. T. 1980, in IAU Symp., 86, Radio Physics of the Sun, ed. M. R. Kundu & T. E. Gergely (Dordrecht: Reidel), 141
Fontenla, J. M., Avrett, E. H., & Loeser, R. 1993, ApJ, 406, 319
Gelfreikh, G. B., Makarov, V. I., Tlatov, A. G., Riehokainen, A., & Shibasaki, K. 2002, A&A, 389, 618
Gopalswamy, N., Shibasaki, K., Thompson, B. J., Gurman, J., & DeForest, C. 1999, JGR, 104, 9767
Horne, K., Hurford, G. J., Zirin, H., & de Graauw, T. 1981, ApJ, 244, 340
Iwai, K., & Shimojo, M. 2015, ApJ, 804, 48
Iwai, K., Shimojo, M., Asayama, S., et al. 2017, SoPh, 292, 22
Kosugi, T., Ishiguro, M., & Shibasaki, K. 1986, PASJ, 38, 1
Kurucz, R. L. 1970, SAOSR, 309, 1
Menezes, F., & Valio, A. 2017, SoPh, 292, 195
Nakajima, H., Nishio, M., Enome, S., et al. 1994, IEEEP, 82, 705
Oliveira e Silva, A. J., Selhorst, C. L., Simões, P. J. A., & Giménez de Castro, C. G. 2016, A&A, 592, A91
Pohjolainen, S., Portier-Fozzani, F., & Ragaigne, D. 2000, A&AS, 143, 227
Rozelot, J. P., Kosovichev, A., & Kilcik, A. 2015, ApJ, 812, 91
Selhorst, C. L., Giménez de Castro, C. G., Válio, A., Costa, J. E. R., & Shibasaki, K. 2011, ApJ, 734, 64
Selhorst, C. L., Giménez de Castro, C. G., Varela Saraiva, A. C., & Costa, J. E. R. 2010, A&A, 509, A51
Selhorst, C. L., Silva, A. V. R., & Costa, J. E. R. 2005a, A&A, 433, 365
Selhorst, C. L., Silva, A. V. R., & Costa, J. E. R. 2005b, A&A, 440, 367
Selhorst, C. L., Silva, A. V. R., Costa, J. E. R., & Shibasaki, K. 2003, A&A, 401, 1143
Selhorst, C. L., Simões, P. J. A., Oliveira e Silva, A. J., et al. 2017, ApJ, 851, 146
Shibasaki, K. 1998, in ASP Conf. Ser. 140, Synoptic Solar Physics, ed. K. S. Balasubramaniam, J. Harvey, & D. Rabin (San Francisco, CA: ASP), 373
Shibasaki, K. 2013, PASJ, 65, S17
Simões, P. J. A., Kerr, G. S., Fletcher, L., et al. 2017, A&A, 605, A125
van Hoof, P. A. M., Williams, R. J. R., Volk, K., et al. 2014, MNRAS, 444, 420
Vernazza, J. E., Avrett, E. H., & Loeser, R. 1981, ApJS, 45, 635
Wedemeyer, S., Bastian, T., Brajša, R., et al. 2016, SSRv, 200, 1
White, S. M., Iwai, K., Phillips, N. M., et al. 2017, SoPh, 292, 88
Zirin, H., Baumert, B. M., & Hurford, G. J. 1991, ApJ, 370, 779